*Electrochemical and Solid-State Letters*, **15** (3) A33-A36 (2012)
1099-0062/2012/15(3)/A33/4/$28.00 © The Electrochemical Society


# Three-Dimensional Reconstruction of a $LiCoO_2$ Li-Ion Battery Cathode

**Tobias Hutzenlaub,[z] Simon Thiele,[*] Roland Zengerle, and Christoph Ziegler**

*Laboratory for MEMS Applications, Department of Microsystems Engineering - IMTEK, University of Freiburg, Georges-Koehler-Allee 106, D-79110 Freiburg, Germany*

In the reported work, we reconstruct a $LiCoO_2$ cathode three-dimensionally, for the first time differentiating between all three constituents: (i) active material, (ii) binder and (iii) pore space for this specific material. We apply a hybrid method of manual and gray-scale threshold segmentation to reconstruct a cuboid with a volume of approximately 4500 $\mu m^3$. The reconstructed geometry is characterised to support the data basis of homogenized cathode models. We solve numerically for electrical conductivity and derive electrical tortuosity analytically from the result. Pore space connectivity and pore size distribution are calculated.
 [DOI: 10.1149/2.002203esl] 

Manuscript submitted October 18, 2011; revised manuscript received November 15, 2011. Published December 28, 2011.

Assumptions about the basic microstructure of the battery components form the starting point for most models predicting lithium-ion battery behavior,[1–4] which provide important benchmarking parameters such as cycling performance and temperature characteristics. Until now most models have relied on the porous-electrode theory,[5] which describes potential distribution in both liquid-filled pore space and solid phases by employing concentrated solution theory and Fickian diffusion. Another less common representation of the electrode is the single particle model,[6] in which each electrode is described as a single particle, considerably reducing calculation time. Both approaches have in common that they simplify the actual microstructure to a large degree and neglect effects that can only be explained by considering the inhomogeneous layer with varying pore and particle size.

Recently, focused ion-beam scanning / electron microscopy (FIB/SEM)[7] was employed to study the microstructure of solid oxide fuel cells (SOFCs) by removing thin layers of electrode material and combining images of each layer to produce a three-dimensional reconstruction of the respective electrodes.[8–12] This method was subsequently applied to polymer electrolyte membrane fuel cells (PEMFCs).[13,14]

This technique was also utilized to study the $LiCoO_2$ cathode of a lithium-ion battery, differentiating between the active material and a combined binder and pore phase and focusing on the topography of single $LiCoO_2$ particle, including cracks and grain boundaries.[15] Ender et al.[16] studied a $LiFePO_4$ cathode and identified a spatial distribution of binder, active material and pore volume which differed considerably from a $LiCoO_2$-based cathode. They used the reconstructed microstructure to calculate volume fractions, volume-specific surface areas and tortuosity. Both groups of authors utilize a resin to simplify the segmentation.

Like Wilson et al.,[15] we focus on a $LiCoO_2$ cathode. Unlike them, we differentiate between all three constituent parts - (i) the active material, $LiCoO_2$, (ii) the binder and (iii) the pore space - by applying a hybrid method of manual and gray-scale threshold segmentation. We do not use a resin, which potentially leads to a less invasive method for image generation. After the segmentation process is completed, we generate and mesh a resulting cuboid. In application, we utilize this geometry to calculate the electrical conductivity from bulk values with the finite element method (FEM). Additionally, we calculate connectivity and the distribution of volume and pore size. These parameters are useful for implementation of future models of $LiCoO_2$ cathodes.

## Experimental

To obtain the electrode material used in this work, a new VARTA LIC 18650 WC lithium-ion battery was unsealed and dismantled. After evaporation of the electrolyte, a piece was extracted from the cathode and prepared for FIB/SEM by sputtering a platinum layer onto the surface of the sample to gain a more planar area as a starting point for the FIB. Additionally, two reference lines, one orthogonal and the other with an angle of 48.2° in relation to the cutting plane, were imprinted into the platinum layer, providing a method independent of surface skew or irregularities to determine slice thickness (Fig. 1). With the help of an FEI Quanta three-dimensional dual-beam FIB-SEM at Fraunhofer IZM, Berlin, a cavity was cut into the sample as a starting point and subsequently one side of the cuboid was ablated slice by slice, while the SEM, with an angle of 38° relative to the sample surface, generated one image per slice.

## Image Processing

In a first step, it was verified that the section of the images designated for segmentation contain no crystals that can form during the evaporation of the electrolyte. Then the images were aligned by the following steps: To compensate for global sample movement due to vibrations and temperature-induced contraction and expansion, the images were aligned in reference to an untouched surface area which was visible on all images. With the help of the reference lines, the average slice thickness was determined to be 62 nm ± 12 nm. The chosen resolution of the utilized REM is 35 nm × 35 nm. To compensate for the angled REM, each image was first translated −38.2 nm in the y-direction relative to the preceding image and then stretched by a factor of 1.27 (Fig. 1). The gray-scale images were recalculated to sustain an image resolution of 35 nm × 35 nm with voxels of 35 nm × 35 nm × 62 nm. To complete the alignment process, the images were cropped to remove unwanted fringe areas, such as side walls and surface, generating a stack of 200 images describing a cuboid which measures 20.02 μm × 18.13 μm × 12.4 μm and a volume of approximately 4500 $\mu m^3$.

The segmentation was performed on an image-by-image basis by generating a specific histogram of each image and pre-segmenting the three phases by threshold values given by minima between the overlapping intensity peaks of $LiCoO_2$ and binder phases and left of the binder phase peak. Where required, this segmentation was corrected manually by comparing the pre-segmented images with the original image and its respective neighboring images. This is necessary for material that is visible in the background, but behind the cutting plane, and pixels with a modified gray-scale value due to light reflection from phase boundaries or surface irregularities.

Finally the segmented images were assembled and each phase visualized with the ScanIP software[17] (Fig. 2).

* Electrochemical Society Student Member.
[z] E-mail: tobias.hutzenlaub@hsg-imit.de

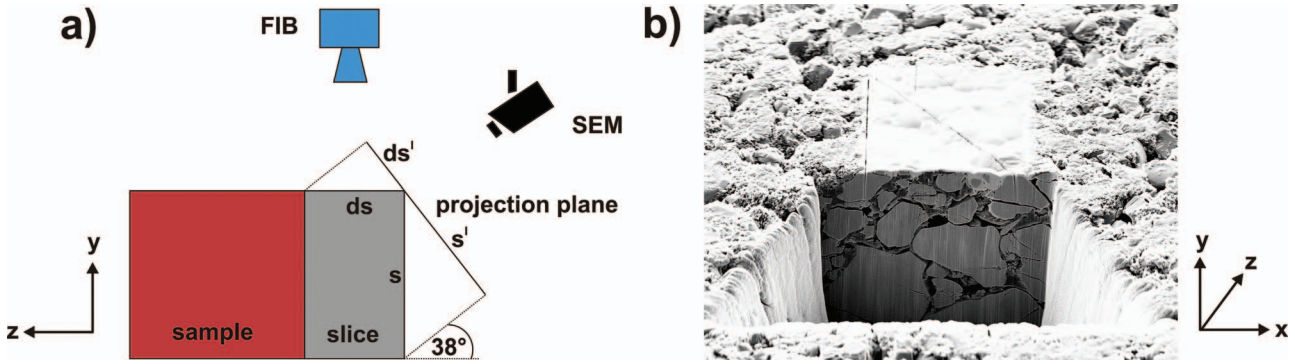


**Figure 1. a)** Schematic diagram of the experimental set-up. The sample is sliced by a focused ion beam. A scanning electron microscope with an angle of 38° relative to the sample surface creates one image per slice. Due to the camera angle, images must be aligned. **b)** Image of cutting plane and sample surface created with the scanning electron microscope. Two reference lines are imprinted into the sputtered platinum layer for alignment purposes.

### Calculation of Material Properties

The importance of the electrical conductivity of the respective electrodes is well documented in the literature.[18–22] In the following, we calculate the specific effective electrical conductivity of the composite electrode in each spatial direction. The governing equation is:

$$i = -\sigma_{eff} \nabla \varphi \qquad [1]$$

with the current density $i$, the effective conductivity $\sigma_{eff}$ of the composite cathode and the electric potential $\varphi$. Assuming the length $L$ from one face of the generated geometry to its opposite side, the corresponding cross-sectional area $A$ and a resulting electric current $I$, we can formulate for all three spatial directions:

$$\sigma_{eff,\kappa} = -\frac{I_\kappa L_\kappa}{\nabla \varphi A_\kappa} \quad \kappa = x, y, z \qquad [2]$$

To solve these equations, we employ the ScanIP software[17] for meshing. Due to the complexity of the geometry, the segmented images were resampled to create one voxel with the dimensions 140 nm × 140 nm × 248 nm from 64 voxels (4 in each spatial direction) by the majority wins method, where the new voxel is assumed to be of the material that was allocated to the majority of its formative voxels.[17] A mesh with 4.2 million cells was created and imported into the FEM software COMSOL.[23] We assume the electrolyte to be non-conductive for electrons. Typical bulk electrical conductivities of $LiCoO_2$: $\sigma_{LiC}$ = 0.0001 $\Omega^{-1}cm^{-1}$[20] and binder with additives: $\sigma_B$ = 0.1 $\Omega^{-1}cm^{-1}$[21,22] are taken from literature. By assuming an arbitrary potential of 1 volt, we can thus numerically solve for the current flow for a specific spatial dimension and then derive the value of the respective electrical conductivity (Table I).

Numerous definitions of tortuosity have been formulated by scientists to describe the effect of porous media on bulk diffusivity values of the materials involved.[24–26] Wyllie et al. and others[24,27,28] verified the equivalence of diffusivity and electrical conductivity. Most models that describe electrical conductivity in porous media rely on a so-called resistivity formation factor $F$.[24,25,29] To evaluate the tortuosity $\tau$ of the geometry reconstructed in this work, we employ an electrical resistivity model that was first introduced by Cornell et al.[29]:

$$\tau_\kappa = F_\kappa \varepsilon \qquad \kappa = x, y, z \qquad [3]$$

with $\varepsilon$ being the porosity of the porous material. In our case, we differentiate between conductive and nonconductive materials, thus defining porosity as the pore-space fraction:

$$\varepsilon = \frac{V_p}{V} \qquad [4]$$

The resistivity formation factor $F$ can be formulated as

$$F_\kappa = \frac{\sigma_{eff,\kappa}}{\sigma_s} \qquad \kappa = x, y, z \qquad [5]$$

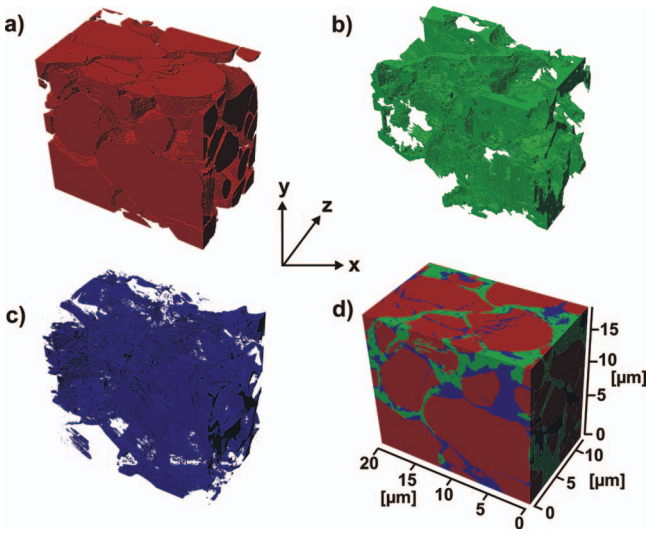


**Figure 2.** Visualization of the three-dimensional reconstruction of a 20.02 µm × 18.13 µm × 12.4 µm section of a lithium-ion cathode with ScanIP. **a)** $LiCoO_2$ **b)** Binder **c)** Pore space **d)** The combination of the three phases.

**Table I. Calculated values of the model in this paper. The main results (effective electrical conductivity, tortuosity and porosity) are emphasized by bold lettering. We achieve good agreement between all three spatial directions, which is an indication of overall isotropy of the cathode material.**

| | x-direction | y-direction | z-direction |
|---|---|---|---|
| $I$ ($\mu A$) | 3.06 | 4.49 | 9.46 |
| $A$ ($\mu m^2$) | 224.8 | 248.3 | 363 |
| $L$ ($\mu m$) | 20.02 | 18.13 | 12.4 |
| $\sigma_{eff}$ ($\Omega^{-1}$ $cm^{-1}$) | **0.00272** | **0.00328** | **0.00323** |
| $\tau$ | **0.0236** | **0.0284** | **0.028** |
| $V_{LiC}$ ($\mu m^3$) | $V_B$ ($\mu m^3$) | $V_P$ ($\mu m^3$) | $V$ ($\mu m^3$) |
| 3159 | 771 | 593 | 4523 |
| $V_{LiC}$ / $V$ | $V_B$ / $V$ | $\varepsilon = V_p$ / $V$ | $\sigma_s$ ($\Omega^{-1}$ $cm^{-1}$) |
| 0.7 | 0.17 | 0.13 | 0.00197 |

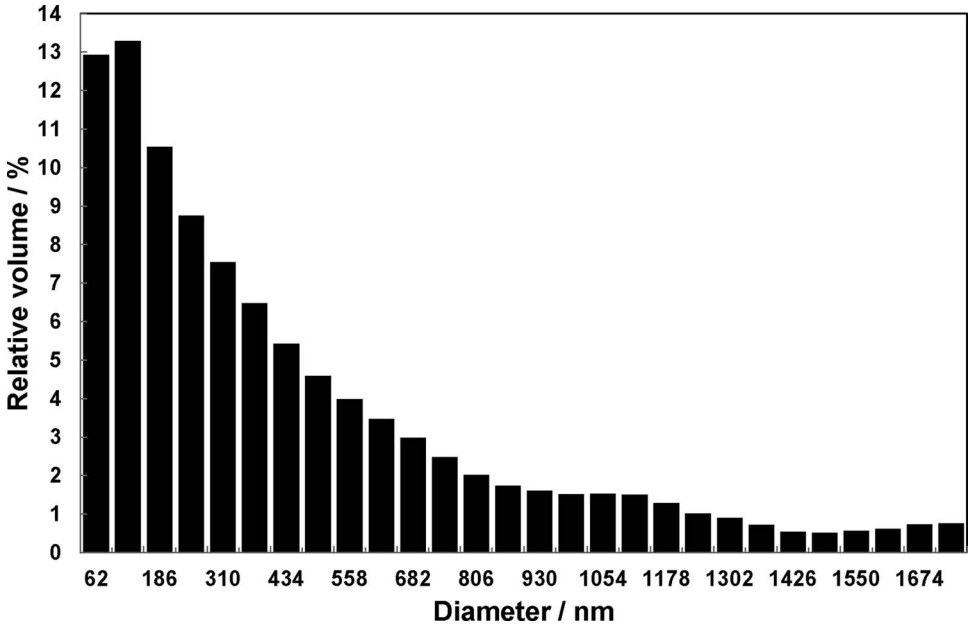


**Figure 3.** Pore size distribution of the connected pores. The x-axis labeling indicates the maximum diameter of the specific interval.

with a conductivity $\sigma_s$ weighted according to the volume fraction of the solid phases, namely binder and $LiCoO_2$:

$$\sigma_s = \frac{\sigma_B V_B + \sigma_{LiC} V_{LiC}}{V_B + V_{LiC}} \quad [6]$$

All volume fractions are calculated with ScanIP.[17] This enables us to derive the electrical tortuosity for all three spatial directions. The results are listed in Table I. Good agreement between all three spatial directions is found, indicating overall isotropy of the cathode material.

To further analyze the $LiCoO_2$-based cathode, we calculate a pore size distribution using a method first described by Delerue et al.,[30] which was further developed by Thiele et al.[14] and smoothed by a kernel density estimation[32] with a Gaussian kernel and a bandwidth of one pixel. In a first step, the pore space is evaluated for connectivity with Matlab.[14,31] The connected pores are determined to account for 96% of the total pore space. In the following step, the x-direction and y-direction of each image is recalculated to give a resolution of 31 nm $\times$ 31 nm while the z-direction is held constant at 62 nm, as the method demands an integral multiplier between resolutions in all three spatial directions. Finally the pore size distribution is calculated. The result is depicted in Fig. 3. A large number of pores were found between 0 and 186 nm which – in addition to effects due to the method employed[14] - are also attributed to the numerous small pores in the binder material. This leads to the conclusion that in future work, the binder material must be analyzed with a higher resolution, as its morphology is on a different scale to the distribution of $LiCoO_2$ particles.

## Conclusions

In the reported work, the three-dimensional reconstruction method was utilized for the first time to identify and differentiate between all three phases of the $LiCoO_2$-based cathode of a Li-ion battery. This is needed to replace simpler models such as the porous-electrode theory, so that geometrical characteristics of the studied material can be represented more exactly. As an example, we characterize the cathode in terms of electrical conductivity and pore size distribution to improve on the data base of homogenized cathode models. To support future meso-scale models, we provide the segmented images as supplementary material. Please contact the corresponding author for more information on how to acquire these images.

## Acknowledgment

The authors acknowledge the collaboration with Fraunhofer IZM, Berlin.

## List of Symbols

| | |
|---|---|
| $A$ | *cross-sectional area of the reconstructed, cuboidal cathode section* ($\mu m^2$) |
| $F$ | *resistivity formation factor* |
| $i$ | *electric current density* ($A\ \mu m^{-1}$) |
| $I$ | *electric current (A)* |
| $L$ | *distance between two opposite faces of the reconstructed, cuboidal cathode section* ($\mu m$) |
| $V$ | *volume of the reconstructed, cuboidal cathode section* ($\mu m^3$) |
| $V_B$ | *volume of the binder phase* ($\mu m^3$) |
| $V_{LiC}$ | *volume of the* $LiCoO_2$ phase ($\mu m^3$) |
| $V_P$ | *volume of the pore space* ($\mu m^3$) |
| $\Delta\varphi$ | *electric potential difference (V)* |
| $\varepsilon$ | *porosity* |
| $\kappa$ | *subscript defining spatial direction* |
| $\sigma_B$ | *bulk conductivity of the binder material with conductivity-enhancing additives* ($0.1\ \Omega^{-1}cm^{-1}$) |
| $\sigma_{eff}$ | *effective conductivity of the composite cathode* ($\Omega^{-1}cm^{-1}$) |
| $\sigma_{LiC}$ | *bulk conductivity of the active material* $LiCoO_2$ ($0.0001\ \Omega^{-1}cm^{-1}$) |
| $\sigma_s$ | *combined bulk conductivity of the solid phases, binder and* $LiCoO_2$, *weighted according to respective volume fraction* ($\Omega^{-1}cm^{-1}$) |
| $\tau$ | *tortuosity* |
| $\varphi$ | *electric potential (V)* |

## References

1. P. Arora, R. E. White, and M. Doyle, *Journal of The Electrochemical Society*, **145**, 3657 (1998).
2. G. G. Botte, V. R. Subramanian, and R. E. White, *Electrochimica Acta*, **45**, 2595 (2000).
3. P. M. Gomadam, J. W. Weidner, R. A. Dougal, and R. E. White, *Journal of Power Sources*, **110**, 267 (2002).
4. S. Santhanagopalan, Q. Guo, P. Ramadass, and R. E. White, *Journal of Power Sources*, **156**, 620 (2006).
5. J. Newman and W. Tiedemann, *AIChE Journal*, **21**, 25 (1975).

6. G. Ning and B. N. Popov, *Journal of The Electrochemical Society*, **151**, A1584 (2004).
7. L. Holzer, F. Indutnyi, P. H. Gasser, B. Munch, and M. Wegmann, *Journal of Microscopy*, **216**, 84 (2004).
8. J. R. Wilson, W. Kobsiriphat, R. Menzona, H. Y. Chen, J. M. Hiller, D. J. Miller, K. Thornton, P. W. Voorhees, S. B. Adler, and S. A. Barnett, *Natural Materials*, **5**, 541 (2006).
9. J. Joos, T. Carraro, A. Weber, and E. Ivers-Tiffée, *Journal of Power Sources*, **196**, 7302 (2011).
10. D. Gostovic, J. R. Smith, D. P. Kundinger, K. S. Jones, and E. D. Wachsman, *Electrochemical and Solid-State Letters*, **10**, B214 (2007).
11. J. R. Wilson, A. T. Duong, M. Gameiro, H. Y. Chen, K. Thornton, D. R. Mumm, and S. A. Barnett, *Electrochemistry Communications*, **11**, 1052 (2009).
12. J. R. Wilson, J. S. Cronin, A. T. Duong, S. Rukes, H. Y. Chen, K. Thornton, D. R. Mumm, and S. Barnett, *Journal of Power Sources*, **195**, 1829 (2010).
13. C. Ziegler, S. Thiele, and R. Zengerle, *Journal of Power Sources*, **196**, 2094 (2011).
14. S. Thiele, R. Zengerle, and C. Ziegler, *Nano Research*, **4**, 849 (2011).
15. J. R. Wilson, J. S. Cronin, S. A. Barnett, and S. J. Harris, *Journal of Power Sources*, **196**, 3443 (2011).
16. M. Ender, J. Joos, T. Carraro, and E. Ivers-Tiffée, *Electrochemistry Communications*, **13**, 166 (2011).
17. www.simpleware.com, 2011.
18. C. W. Wang, A. M. Sastry, K. A. Striebel, and K. Zaghib, *Journal of The Electrochemical Society*, **152**, A1001 (2005).
19. R. Dominko, M. Gaberscek, J. Drofenik, M. Bele, and S. Pejovnik, *Electrochemical and Solid State Letters*, **4**, A187 (2001).
20. M. Park, X. Zhang, M. Chung, G. B. Less, and A. M. Sastry, *Journal of Power Sources*, in press, doi: 10.1016/j.jpowsour.2010.06.060 (2010).
21. D. Guy, B. Lestriez, R. Bouchet, and D. Guyomard, *Journal of The Electrochemical Society*, **153**, A679 (2006).
22. G. Liu, H. Zheng, S. Kim, Y. Deng, A. M. Minor, X. Song, and V. S. Battaglia, *Journal of The Electrochemical Society*, **155**, A887 (2008).
23. www.comsol.com, 2011.
24. M. R. J. Wyllie and M. B. Spangler, *AAPG Bulletin - American Association of Petroleum Geologists*, **36**, 359 (1952).
25. W. O. Winsauer, H. M. Shearin, P. H. Masson, and M. Williams, *AAPG Bulletin - American Association of Petroleum Geologists*, **36**, 253 (1952).
26. G. Dogu and J. M. Smith, *AIChE Journal*, **21**, 58 (1975).
27. W. H. Hedley, F. J. Lavacot, S. L. Wang, and W. P. Armstrong, *AIChE Journal*, **12**, 321 (1966).
28. A. A. Garrouch, L. Ali, and F. Qasem, *Industrial and Engineering Chemistry Research*, **40**, 4363 (2001).
29. D. Cornell and D. L. Katz, *Industrial and Engineering Chemistry*, **45**, 2145 (1953).
30. J. F. Delerue, E. Perrier, Z. Y. Yu, and B. Velde, *Physics and Chemistry of the Earth Part A - Solid Earth and Geodesy*, **24**, 639 (1999).
31. www.mathworks.com, 2011.
32. M. Rosenblatt, *Annals of Mathematical Statistics*, **27**, 832 (1956).